

AD-A084 267

CAMBRIDGE UNIV (ENGLAND) CAVENDISH LAB F
LIQUID IMPACT EROSION MECHANISMS IN TRANSPARENT MATERIALS.(U)
NOV 79 J E FIELD; M J MATTHEWSON; S V ZWAAZ AFOSR-78-0125

F/6 17/5

UNCLASSIFIED

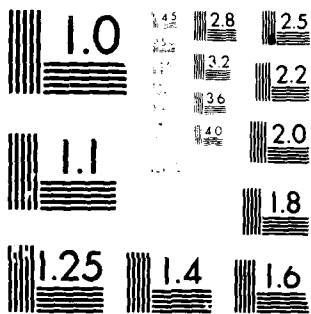
AFWAL -TR-80-4057

NL

1 of 1
 ΔE
 6(1) 10(1) 10(1)

THE
OFFICIAL
OF THE
1998-99

END
DATE
FILMED
6-80
DTIC



MICROCOPY RESOLUTION TEST CHART
NATIONAL BUREAU OF STANDARDS-1963-A

ADA 084267

AFWAL-TR-80-4057

②

LEVEL

LIQUID IMPACT EROSION MECHANISMS IN TRANSPARENT MATERIALS

UNIVERSITY OF CAMBRIDGE
CAVENDISH LABORATORY
CAMBRIDGE, ENGLAND

DTIC
ELECTE
MAY 19 1980
S D E

NOVEMBER 1979

TECHNICAL REPORT AFWAL-TR-80-4057
Interim Report for period September 1978 — September 1979

Approved for public release; distribution unlimited.

DDC FILE COPY

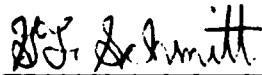
MATERIALS LABORATORY
AIR FORCE WRIGHT AERONAUTICAL LABORATORIES
AIR FORCE SYSTEMS COMMAND
WRIGHT-PATTERSON AIR FORCE BASE, OHIO 45433

80 5 19 128

NOTICE

When Government drawings, specifications, or other data are used for any purpose other than in connection with a definitely related Government procurement operation, the United States Government thereby incurs no responsibility nor any obligation whatsoever; and the fact that the government may have formulated, furnished, or in any way supplied the said drawings, specifications, or other data, is not to be regarded by implication or otherwise as in any manner licensing the holder or any other person or corporation, or conveying any rights or permission to manufacture, use, or sell any patented invention that may in any way be related thereto.

This technical report has been reviewed and is approved for publication.

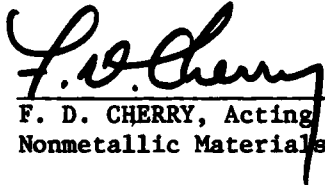


G. F. SCHMITT
Project Engineer



W. C. KESSLER, CHIEF
Coatings & Thermal Protective
Materials Branch

FOR THE COMMANDER



F. D. CHERRY, Acting Chief
Nonmetallic Materials Division

"If your address has changed, if you wish to be removed from our mailing list, or if the addressee is no longer employed by your organization, please notify AFWAL/MLBE, W-PAFB, OH 45433 to help us maintain a current mailing list.

Copies of this report should not be returned unless return is required by security considerations, contractual obligations, or notice on a specific document.

19 REPORT DOCUMENTATION PAGE		READ INSTRUCTIONS BEFORE COMPLETING FORM
1. Report Number 13 AFWAL-TR-80-4057	2. Govt Accession No. ADA084 267	3. Recipient's Catalog Number
4. Title (and Subtitle) Liquid Impact Erosion Mechanisms in Transparent Materials.	5. Type of Report & Period Covered Interim Scientific Report 30 Sep 78-30 Sep 79	6. Performing Org. Report Number
7. Author(s) J.E. Field / M.J. Matthewson / S. van der Zwaag	8. Contract or Grant Number AFOSR-78-00125, AFOSR-78-3705	
9. Performing Organization Name and Address Physics and Chemistry of Solids Cavendish Laboratory Madingley Road Cambridge CB3 0HE UK	10. Program Element, Project, Task Area & Work Unit Numbers FY 1457-78-00125 2422/01	
11. Controlling Office Name and Address OSR(PKN) Bolling AFB DC 20332	12. Report Date 11 November 79	
14. Monitoring Agency Name and Address AFML/MBE, Wright-Patterson AFB Oh 45433	13. Number of Pages 24	
15. 12/48		
16. & 17. Distribution Statement Approved for public release; distribution unlimited.		
18. Supplementary Notes		
19. Key Words liquid impact, erosion, fracture, high-speed photography, zinc sulphide, zinc selenide, silicon nitride.		
20. Abstract A study has been made of damage mechanisms caused by liquid drop impact on various infra-red transparent solids. Techniques are described for producing liquid jets which simulate the damage produced by impact with spherical drops. Advantages of this approach are the simplicity of the experimentation, the low construction cost and the broad range of drop size and velocity which can be covered. A hydraulic strength measuring apparatus for brittle materials is described which allows "residual strengths" to be measured. Materials examined in this report include silicon nitride, zinc sulphide and zinc selenide.		

FOREWORD

This report summarizes research performed at the Cavendish Laboratory, University of Cambridge, Cambridge, England from September 1978 through September 1979 under AFOSR Grant 78-3705. The work was initiated with Laboratory Directors Discretionary Funds, P.E. 61102F and subsequently funded with Project 2422 "Protective Coatings and Materials", Task No. 242201 "Coatings for Aircraft and Spacecraft". The report was submitted in March 1980.

Accession For	
NTIS GRA&I	<input checked="checked" type="checkbox"/>
DDC TAB	<input type="checkbox"/>
Unannounced	<input type="checkbox"/>
Justification	
By _____	
Distribution/ _____	
Availability Codes	
Dist	Avail and/or special
A	

CONTRACT/GRANT NUMBER : AFOSR-78-3705

LIQUID IMPACT EROSION MECHANISMS IN TRANSPARENT MATERIALS

Dr. J.E. Field, Dr. M. Matthewson and S. van der Zwaag

Physics and Chemistry of Solids
Cavendish Laboratory
Madingley Road
Cambridge CB3 0HE UK

INTERIM SCIENTIFIC REPORT: 30th September 1978 - 30th September 1979

Approved for public release : distribution unlimited.

Prepared for AFML/MBE, Wright-Patterson AFB, OH 45433, U.S.A.

and

European Office of Aerospace Research, London, England.

TABLE OF CONTENTS

	<u>page</u>
INTRODUCTION	1
1. THE JET METHOD	2
Nozzle design	2
Liquid jet impact on PMMA	4
Jet structure	5
Jet velocity calibration	6
2. AN IMPROVED STRENGTH MEASURING TECHNIQUE FOR BRITTLE MATERIALS	8
Theory of hydraulic test apparatus	9
Experimental	11
The residual strength of silicon nitride	13
Conclusions	15
Notation	16
3. ZINC SULPHIDE, ZINC SELENIDE	17
Single impact	18
Multiple impact	19
4. CONCLUSIONS	19
FIGURE CAPTIONS	21
REFERENCES	24

INTRODUCTION

On this project we are interested in assessing the damage caused by liquid drop impact on infra-red transparent solids. In recent work we have been using three different techniques for studies of high velocity liquid/solid impact. The first involves projecting specimens of up to 25.4 mm diameter against stationary drops. The second fires liquid jets at a stationary target. The third uses 2-d liquid configurations (discs, wedges of liquid) which are impacted. The first experiment is nearest to the practical situation in rain erosion, the second has distinct advantages in its ease of operation, low construction cost, and the velocity range which can be covered. The final approach, using 2-d configurations, allows processes occurring inside the impacted liquid to be followed by high-speed photography, and is also nearer situations which can be theoretically analysed. The first part of this report describes recent developments with the jet method.

Since the early 1970's we have attempted to place damage assessment on a sounder quantitative basis by measuring "residual strengths". This involves impacting a specimen under known conditions and then measuring the strength. A hydraulic apparatus, which stresses 2" diameter disc specimens, was developed for this work (Gorham and Rickerby, 1975, Matthewson, 1978). In recent work we have improved this technique. The new design greatly reduces the number of specimens which fail at their edge and reduces the scatter in results. To complement this, a more detailed theory is developed to analyse results. An investigation of the strength of silicon-nitride as a function of the impact velocity of a water jet illustrates the use of the apparatus. A method of converting fracture stress data to equivalent flaw size data is given which allows a more physically meaningful and useful presentation of results. This work is discussed in part two.

Zinc sulphide and zinc selenide are both materials which have useful infra-red transmitting properties. Specimens have been impacted by jets from 0.4 and 0.8 mm nozzles and the results are presented in the third part of this report.

1. THE JET METHOD

This technique (see figure 1) was pioneered in this laboratory by Brunton (1959). In early research it was used qualitatively to evaluate liquid impact mechanisms. However, in recent years Field et al. (1974, 1976, 1979) have researched to place it on a sounder quantitative basis. It is now possible to produce jets which give essentially similar damage to impacts with spherical drops. In this work the nozzle shown in figure 2 was used. Different sized jets can be produced by changing the value of the orifice diameter d . In some situations it is advantageous to fill the nozzle to position E in others to position F. The 0.4 mm nozzle produces jets which simulate drops of ~ 2 mm diameter for a wide range of velocities. The nozzles with larger values of d were able to give "equivalent" drop sizes up to many millimeters diameter. Full details can be found in the references given.

An advantage of the nozzle of figure 2 is its basic simplicity and the fact that a wide range of jet sizes can be obtained merely by changing d . However, this overall capability means that the nozzle is not optimized for any particular size. We decided therefore to concentrate on finding the best nozzles for the low end of the d range (0.4 and 0.8 mm nozzles) since these simulate 2 mm and 4 mm diameter drops for a wide velocity range (see figure 3).

Nozzle design

The formation of the jet by the extrusion process is governed by the following parameters: (i) diameter and length of the chamber, (ii) transition from chamber to orifice, (iii) diameter of the orifice and (iv) length of the orifice. The entrance diameter of the chamber is determined by the 0.22 calibre air gun. Chamber diameter and length determine the volume of water which is accelerated. The diameter of the orifice is an independent

variable which can be changed to produce jets of the required diameters. The two remaining variables of the nozzle, the transition between chamber and the length of the orifice, govern the stability of the extruded jet.

Nozzle designs made by Brunton are shown in figure 4. Jets made with nozzles type a and c appeared to be stable. Results for type c were slightly better due to the longer orifice section, which tends to stabilise the jet. This type of nozzle, mainly with a 1.6 mm diameter orifice, was adopted as the standard for liquid impact studies in this laboratory (Brunton 1959, Field 1962, Camus 1971, Gorham 1974, Rickerby 1976). Nozzles of type d gave rise to very unstable jets. Also jets from type b nozzles showed a marked lack of coherence. This is thought to be caused by insufficient damping of the radial velocity components in the relatively short orifice section. The behaviour of similar nozzle types during continuous production of water jets is reported to be very good (Leach and Walker 1966, Kinoshita 1976).

The new nozzle designs for small orifice diameters are shown in figure 5. The transition between chamber and orifice is now more gradual to minimise turbulence in the jet. The corners are rounded except the exit corner which is sharp. All the internal surfaces are polished. Nozzles are made from stainless steel to preserve the good surface quality during prolonged operation.

Indirect evidence for the lower flow resistance of the new nozzle types comes from the deformation of the nozzle. The chamber wall of the traditional nozzle suffered from plastic deformation (with a measurable change in the chamber's external dimensions) at firing pressures of 2.8 MPa for the 0.8 mm orifice and at 2.0 MPa for the 0.4 mm orifice. Plastic deformation was undetectable for nozzles with a 45° or a curved transition up to firing pressures of 3.5 MPa, indicating that lower hydrostatic pressures are developed in the more freely flowing fluid.

Liquid jet impact on PMMA

The most important feature of the liquid jets produced by the Brunton nozzle is the resemblance between the damage produced by liquid jet impact and the damage produced by liquid drop impact. One way to make a selection between different nozzle types is therefore to study the impact damage produced by the jets on a well known material with uniform surface conditions, such as polymethylmethacrylate (PMMA).

The damage produced by liquid jet impact on PMMA exhibits a central plateau of undamaged material surrounded by an annular crater. Subsurface damage can occur at high velocities due to localised shear.

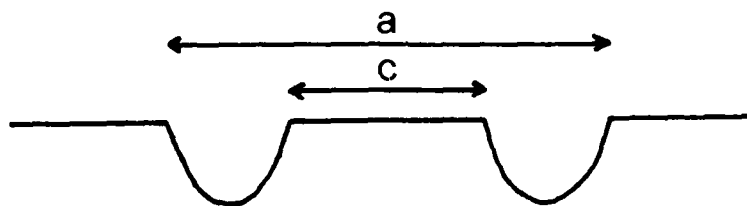


Fig. 6 Nomenclature for damage site dimensions.

A diagram for the nomenclature of the damage site dimensions is shown in figure 6. The inner and outer diameter of the crater were measured optically and are plotted in figure 7 for the 0.8 mm nozzles with curved (a new nozzle, fig. 5b) and 60° (old nozzle, fig. 2) transitions. Data for the 45° nozzle (fig. 5a) are not illustrated, but were similar to those for the curved nozzle. The scatter* was smaller for both types of new nozzle. Figure 7a gives the results for the "old" 60°

* In order to give a good visual presentation of the improvement, the data have not been treated statistically; the points plotted are the mean of 10 experiments, and the bars mark the limits of values for the crater dimensions.

nozzle, and 7b for the new curved nozzle. No difference in damage quality between nozzles with 45° and curved transition was detected, but the greater resistance to plastic deformation makes the curved transition between chamber and orifice preferable.

For the 0.4 mm nozzles, the damage produced by the new 45° nozzle was more symmetric and reproducible than the damage produced by the earlier 0.4 mm 60° nozzle (fig. 2). The maximum firing pressure before the onset of plastic deformation of the nozzle was 3.5 MPa for the 45° transition and 2.0 MPa for the 60° transition.

A longer orifice section, 5 mm instead of 2 mm, for the 0.4 mm nozzle with the 45° transition (fig. 5c) gave no further improvements. Since it is more difficult to manufacture it has not been adapted for general use.

With the 0.4 mm orifice the "curved" type nozzle is also difficult to manufacture reproducibly and easily. For future work, the 45° type nozzle (figure 5a) has been chosen for 0.4 mm jets and the "curved" nozzle (figure 5b) for 0.8 mm jets.

Jet structure

The shape of the jets made by the new nozzle types was studied with high speed photography using the single shot Beckman and Whitley camera (Model 511). The jet was illuminated by a 150 ns Beckman and Whitley point light source (Model 5401). An example for a jet from a 0.8 mm nozzle is given in figure 8. The shape of the 'umbrella' of droplets around the central core of the jet is determined partly by the amount of water in the orifice section prior to firing and partly to aerodynamic effects. A large amount of water in the orifice section increases the dimensions of this 'umbrella'. Measurements of the damage sites produced by the impact of the liquid jets on PMMA showed that these surrounding droplets do not affect the dimensions of the damage. Comparison of the dimensions of the

jet and the resulting impact damage confirmed that the central undamaged plateau has the same diameter as the jet core at the moment of impact.

Jet velocity calibration

An Imacon electronic framing image converter camera was used to measure the velocity of the jets as a function of distance from the orifice exit and of firing pressure for the best nozzle types. The higher rate of data accumulation makes the Imacon camera more suitable for the production of calibration curves than a system consisting of two Beckman and Whitley single shot cameras combined by a beamsplitter, although the accuracy of the latter system is slightly higher.

Examples of the movement of the head of the jet as recorded by the Imacon are shown in figure 9 for 1.6, 0.8 and 0.4 mm nozzle sizes. In all cases the jet head is smooth and slightly curved. This is why they simulate drop impact so well. The black lines on the pictures are from a grid placed behind the jet and serve as fiducial marks.

Jet velocities as a function of distance from the orifice exit are plotted in figures 10, 11 and 12 for the three types of nozzles investigated. The jets appear to accelerate very quickly during the first millimetres of flight, but then reach steady values. In our experiments a "stand-off" distance of 10 mm is used. At this stage, a steady plateau has been reached. The resemblance between the curves is very high, indicating that the process which governs the velocity as a function of flight distance is independent of orifice diameter and of the transition between chamber and orifice. The volume of water in the orifice prior to firing does not influence the velocity to a measurable extent. Consequently the measured behaviour of the jet is not a result of the 'dead' water in the orifice but of the inertia of the total water volume in the nozzle.

The maximum stand-off distance that could be used is limited by the

aerodynamic distortion of the jet. No aerodynamic disruption of the jet was found for the nozzle with curved transition and 0.8 mm orifice diameter in the 20 mm of flight investigated. Taylor instabilities eventually break up the jet. Experimental and theoretical work on this is described by Field and Lesser (1977).

The velocity at 10 mm standoff distance as a function of firing pressure is plotted in figures 13 and 14 for the two new nozzle types which have been adopted. The calibration curves for the original 0.4 and 0.8 mm orifice 60° nozzles (fig. 2) are also included (data from Rickerby 1976). The curves for the new nozzles are slightly lower but produce jets more reproducibly as discussed earlier.

Figures 13 and 14 are for experiments with the set-up as in figure 1 with the projectile impacting directly against the neoprene disc. With such small orifices the jet velocity, even for the lowest firing pressures which can conveniently be used, are still high and well above the damage thresholds for most materials. In earlier work, we used the idea of a "momentum exchanger" so that lower velocity jets could be obtained (Field et al. 1974). Figure 15 illustrates the arrangement using a simple cylinder as the momentum exchanger. A recent modification has been to add a block as shown in figure 16. The effect on jet velocity for both 0.4 mm and 0.8 mm nozzles is given in figures 17 and 18. The curves 1 to 4 are successively, 1 without any form of momentum exchanger, 2 with the cylinder as momentum exchanger, 3 with the cylinder plus an aluminium block and 4 with the cylinder plus a steel block. The block dimensions were (12 × 12 × 21 mm). This now gives us minimum velocities down to about 125 m s⁻¹ for the 0.4 mm nozzle and 90 m s⁻¹ for the 0.8 mm nozzle which are less than the threshold damage velocities for most of the materials we are interested in. If necessary, it would be a simple matter to obtain even lower velocities. In all cases, the calibration curves were obtained using the Imacan high-speed camera.

2. AN IMPROVED STRENGTH MEASURING TECHNIQUE FOR BRITTLE MATERIALS

In recent years there has been a growing interest in assessing impact, wear and indentation damage to a specimen in terms of strength loss or flaw growth. Gorham and Rickerby (1975) described a strength test apparatus in which a circular disc specimen is supported near its edge and is burst by hydraulic pressure applied to one side. The fracture stress may be calculated from the bursting pressure. Their paper discusses the advantages this technique has over other methods which are available; in particular, the fraction of specimens which fail at the support or the edge is comparatively low. While the Gorham and Rickerby apparatus has a relatively low frequency of edge failures, Rickerby (1977) has found that for 25mm radius glass disc edge failures are not insignificant: some 15% of 3mm thick and 25% of 6mm thick specimens fail in this way. Our work with this test shows that failures of this sort occur at the support, rather than the edge, and are due to a large tensile circumferential stress component (equal to about one-half the stress at the centre of the disc) interacting with local stress concentrations caused by support irregularities. Figure 19 illustrates specimens which failed (a) at the support and (b) away from the support.

The hydraulic test approach has already provided useful results in assessing impact damage and erosion parameters of a variety of brittle materials (Field et al 1974, 1979a, 1979b, Rickerby 1977). Specimens of some materials are often in short supply and extremely costly and wasting a proportion of them by support failure is undesirable. The motivation for the present work was to reduce the problem of support failures.

This report describes a modified hydraulic tester where the support ring radius is reduced giving an acceptably low frequency of support failures. The stress distributions across the disc which have been used previously are not accurate in this situation and a new distribution is derived theoretically. The use of the new apparatus is illustrated by measurements of the strength of silicon nitride discs after impact by water jets. These results are then interpreted in terms of equivalent induced flaw sizes which are physically more meaningful.

The notation used is given at the end of this section.

Theory of hydraulic test apparatus

A scale schematic diagram of the apparatus is shown in Figure 20. The specimen of radius r_2 is supported by a ring of radius r_1 and a uniform pressure is exerted on the disc via a neoprene diaphragm by a hydraulic system. Gorham and Rickerby used values of $r_2 = 25\text{mm}$ and $r_1 = 23\text{mm}$. The stress distribution for a disc simply supported at its edge is given by Timoshenko (1940) and is fairly accurate in this case. Mansfield (1963) gives a more appropriate distribution which allows for the stiffening effect of the overhang of the disc over the support, but does not account for the pressure applied to the overhang.

Timoshenko (1940) gives the differential equation for the displacements, $w(r)$, of a thin circular plate under an axially symmetric pressure distribution, $q(r)$:

$$\frac{1}{r} \frac{d}{dr} \left[r \frac{d}{dr} \left(\frac{1}{r} \frac{d}{dr} \left(r \frac{d}{dr} w(r) \right) \right) \right] = \frac{q(r)}{D'} \quad (1)$$

In this case $q(r) = P$, the uniform applied pressure, giving a general solution to (1):

$$w(r) = \frac{Pr_1^4}{64D} \{ A + B \ln(r/r_1) + C(r/r_1)^2 + D(r/r_1)^2 \ln(r/r_1) + (r/r_1)^4 \} \quad (2)$$

Two sets of values for the coefficients A, B, C and D may be found corresponding to the solutions for $r > r_1$ and $r < r_1$ by using the boundary conditions given by Mansfield (1963). From the results the stress distribution on the surface of the disc may be found.

$$\sigma_r = \frac{3Pr_1^2}{8t^2} \left\{ \rho^2 \left[3\nu + 1 - 4(1 + \nu) \ln(\rho) \right] + 2(1 - \nu) - (3 + \nu) \xi^2 \right\}$$

and (3)

$$\sigma_\theta = \frac{3Pr_1^2}{8t^2} \left\{ \rho^2 \left[3\nu + 1 - 4(1 + \nu) \ln(\rho) \right] + 2(1 - \nu) - (1 + 3\nu) \xi^2 \right\}$$

for $r < r_1$. These equations reduce to those of Timoshenko when $r_1 = r_2$.

Figure 21 shows the radial distribution of these stresses for various values of r_1/r_2 . The stresses are normalised to the central stress when $r_1/r_2 = 1$: effectively they are the stress distributions for a fixed applied pressure but differing support ring radii. As r_1/r_2 decreases, the magnitude of the circumferential stress at the support decreases with respect to the central stress, decreasing the probability of a support failure. However, the central stress also decreases with r_1/r_2 . This implies that to reach a certain stress level at the centre of the disc, the hydrostatic pressure must be increased as r_1/r_2 decreases. Hence, as r_1/r_2 decreases, the contact pressure at the support increases if a fixed central stress is to be obtained. If r_1/r_2 is near unity the circumferential stress component is large but if r_1/r_2 is small a large contact pressure results. In order to minimise the number of support failures a compromise value for r_1/r_2 must be chosen and a value of 0.8 has been found to be suitable.

This gives a reduction in the circumferential stress component of ~30% with respect to support at the edge, although the contact pressures are doubled. The circumferential stress is more important than the contact pressure, as the overall effect is found experimentally to reduce the number of support failures. Experiments on 6mm thick glass discs show that with $r_2 = 25\text{mm}$ and $r_1 = 20\text{mm}$ 5% fail at the support compared with 25% for $r_1 = 23\text{mm}$. At this level support failures may be safely ignored.

Timoshenko gives a correction term which should be added to the displacements, $w(r)$, which takes into account the effect of shear within the plate and the lateral extension due to the applied pressure. Additional tensile stress components $\Delta\sigma_r$ and $\Delta\sigma_\theta$ can readily be calculated from the correction term and reduced to:

$$\Delta\sigma_r = \Delta\sigma_\theta = \frac{(3 + \nu)}{4(1 - \nu)} P \quad (4)$$

The fracture stress, σ_f , may be calculated using

$$\sigma_f = \sigma_r \sin^2 \phi + \sigma_\theta \cos^2 \phi$$

where P takes the value of the bursting pressure, r is the distance between the fracture origin and the centre of the disc and ϕ is the angle between the fracture origin and the radius vector.

Experimental

The theoretically derived stress distribution has been verified experimentally. Strain gauges (Showa type N22-FA-2 double element resistance gauges) were attached to 3 mm and 6 mm glass discs at various distances from the centre (0, 8 and 16 mm). The discs were loaded in the tester and the strain gauge output was found as a function of applied pressure. From the results the function ϵ/P , where ϵ is the strain, is calculated by linear regression.

Figure 22 compares the experimental and theoretical determinations of the strain distribution across the specimens for both disc thicknesses. The theoretical curves are calculated using equations (3) and (4) and using

$$\begin{aligned}\epsilon_r &= \frac{1}{E} (\sigma_r - \nu\sigma_\theta) \\ \epsilon_\theta &= \frac{1}{E} (\sigma_\theta - \nu\sigma_r)\end{aligned}\tag{5}$$

Equations (5) are derived from the elasticity equations, given that the stress perpendicular to the surface, σ_z , is zero. The values of elastic constants are $E = 69$ GPa and $\nu = 0.25$ (Woodward, 1974). The horizontal error bars are due to uncertainty in positioning the gauges and also that the gauges are of finite size (2 mm) and average the strains over their length. The vertical error bars are estimates of the scatter in the slopes of ϵ versus P plots.

For the 3 mm discs (Figure 22a) the theory fits the measured circumferential strains very well. However, for the radial strains, the fit is good everywhere except near the support ring where the measured strain is ~200% larger than is predicted theoretically. This can be attributed to the stress field due to the line loading at the support interacting with the stress field due to the plate bending. However, this discrepancy is not significant as the great majority of specimens fail near the centre of the disc where there is excellent correlation between theory and experiment.

For the 6 mm discs (Figure 22b) the experimental points lie close to the theory line although they are systematically slightly higher. This error is due to a combination of factors. Firstly, the theory assumes that the thickness is small compared with the width and this is not strictly valid for $r_1 = 20$ mm and $t = 6$ mm.

A full treatment for a thick plate is more complex and has been left for future work. Secondly, deviations caused by stresses at the support are more significant as a greater pressure is needed to generate the same stresses at the centre of a thicker specimen.

The residual strength of silicon nitride

The pressure tester has been used in the past to examine the variation of strength of various materials with the velocity of impacting water jets. The results have application to the studies of rain erosion since the pressure tester technique provides a rapid and inexpensive method of evaluating erosion resistance quantitatively. The impact behaviour of infra-red transparent materials has received much attention in recent years (Field et al. 1974, 1979a, 1979b) and the results of an investigation on hot-pressed silicon nitride (supplied by F.M.I.) are presented here. This type of material is expensive and in short supply. 45 specimens were available for this investigation and consequently wastage of specimens was undesirable. With the modified pressure tester no support failures occurred and each specimen yielded useful information.

The results presented here outline an experimental programme for obtaining data on the impact properties of a material using the pressure tester and other techniques. The methods illustrate not only the use of the tester, but also how the performance of materials may be rapidly evaluated in a quantitative manner. The results can then be used to determine how improvements can be made to material properties.

The silicon nitride discs were impacted centrally by water jets of 3 mm diameter produced by an apparatus which is described fully elsewhere by Bowden and Brunton (1961) and Field et al (1979a). The

discs were then burst in the tester with the impacted surfaces in tension. Parameters used for calculating results are $r_1 = 20$ mm, $r_2 = 25$ mm, $t = 3$ mm and $\nu = 0.27$. Figure 23 shows the results of the fracture stress plotted as a function of jet velocity. Each data point is an average for five specimens. Up to a velocity of 400 m s^{-1} the residual strength remains constant at its unimpacted value. The strength then falls to a constant value between 500 and 700 m s^{-1} . This fall is due to the formation of small circumferential cracks around the impact site by the Rayleigh surface wave (Bowden and Field 1964, Field et al 1979a). Above 700 m s^{-1} the residual strength falls towards zero due to the formation of long radial cracks in the specimen until at $\sim 850 \text{ m s}^{-1}$ the discs are fragmented by the impact. The form of the residual strength curve is well understood and is described elsewhere (e.g. Field et al. 1979b).

Expressing residual strength characteristics in terms of fracture stresses is not a particularly useful way of representing the results as fracture stresses depend not only on fundamental material properties, but also on the ambient environment, the loading system and the loading rate. For this reason, the results are converted to the equivalent flaw sizes which are induced by the impact. When the data are presented in this form the fracture stress may be calculated for any loading condition or environment. In general the flaw sizes may be calculated from the fracture stresses using

$$c = \frac{1}{\alpha} \left(\frac{\sigma_f}{K_{IC}} \right)^2$$

where c is a measure of the flaw size, K_{IC} is the critical stress intensity factor and α is a constant depending on the geometries of the flaw and specimen. The flaws are observed to be of the order of millimetres in length in the surface and are therefore not small compared to the specimen thickness (3 mm). Therefore the flaw may

be modelled by a slot crack of length $2c$ in the surface: in this case α has the value π .

The critical stress intensity factor, K_{IC} , is measured using the indentation technique of Lawn and Fuller (1975) in which a Vickers indenter is loaded onto the specimen until radial cracks form.

Figure 24 shows these cracks schematically. K_{IC} is given by

$$K_{IC} = \frac{XL}{a^{3/2}} \quad ; \quad \chi = \frac{1}{\pi^{3/2} \tan \psi}$$

where L is the applied load and ψ is the indenter semi-angle and a is the length of the radial cracks. Figure 25 shows typical results of a/χ as a function of L giving a value of $K_{IC} = 4.9 \pm 0.3 \text{ MNm}^{-3/2}$. Results for several specimens give a mean value of $K_{IC} = 5.2 \pm 0.3 \text{ MNm}^{-3/2}$. This result agrees well with a value of $4.9 \text{ MNm}^{-3/2}$ obtained by Evans (1978) on the same material using a double cantilever method.

Figure 26 shows the flaw size, c , induced by the impact as a function of impact velocity. For unimpacted specimens $c = 110 \pm 10 \mu\text{m}$. The material is granular in nature with grains of the order of $10 \mu\text{m}$ in diameter and the intrinsic flaws are therefore much larger than the grains. By adjustment of the manufacturing process it should be possible to decrease the flaw sizes to of the order of the grain size thus increasing the strength of the material. This would also have the effect of increasing the damage threshold velocity (400 m s^{-1}) as this is a function of the intrinsic flaw size (Field et al. 1979b)

Conclusions

The advantages of the hydraulic test apparatus are (i) the circularly symmetric stress field (ii) the large proportion of specimen surface tested (iii) the ease and rapidity of operation and (iv) the possibility of miniaturization; we have used specimens down to 25mm in diameter.

The improvement to the pressure tester has reduced the number of specimens which fail at the support to an insignificant level. The technique has now been developed to the stage where results are accurate and reliable enough for the tester to be used commercially as a rapid and inexpensive method for evaluation and quality control of materials.

The use of the tester is illustrated by an investigation of the post-impact strength properties of a hot-pressed silicon nitride in which the features of the modified design result in accurate and reliable data. The fracture stress data have been converted to equivalent flaw size data which is more physically meaningful and has enabled a suggestion for improving the material to be made.

Notation

r_2	-	radius of disc specimen
r_1	-	radius of support ring
t	-	disc thickness
E	-	Youngs modulus of disc material
ν	-	Poisson ratio of disc material
$q(r)$	-	radial distribution of pressure (equal to P , the uniform applied pressure)
$w(r)$	-	radial distribution of displacement of the disc
$\sigma_r(r)$	-	radial stress component at the surface of the disc
$\sigma_\theta(r)$	-	circumferential stress component at the surface of the disc
ϕ	-	angle between radius vector and fracture origin
σ_f	-	fracture stress

$$\rho = r_2/r_1$$

$$\xi = r/r_1$$

$$D' = \frac{Et^3}{12(1 - \nu^2)}$$

3. ZINC SULPHIDE, ZINC SELENIDE

At present there is considerable interest in these materials due to their good infra-red transmitting properties. Figures 27-31 show the results of liquid jet impact with them. In all cases jets from a 0.4 mm nozzle were used. Figure 27a is for a single impact on zinc selenide at 600 m s^{-1} . This we would predict to be equivalent to impact at this velocity with a drop of $\sim 2.4 \text{ mm}$ diameter. The figure shows that there is an undamaged central region surrounded by many short circumferential cracks. There are many similarities with impacts on other brittle materials (Bowden and Field 1964, Bowden and Brunton 1961). Figure 27a illustrates the effect of a second impact near the first; the second impact is at the right. The original damage is not greatly affected but that associated with the second impact is significantly more intense, showing that the first impact had weakened the material to radial distances of about 2 mm.

An enlarged view of the cracked region is given in figure 28a, while figure 28b shows a similar area but for an impact velocity of 250 m s^{-1} . The feature labelled A in the figures identifies the enlarged region. The flow of liquid over the cracks has eroded material from them. As earlier work has shown, there is a surface step across each crack which acts as a site for erosion (Bowden and Brunton 1961, Field 1967).

For comparison figures 29 and 30 give results for zinc sulphide. Again the velocities involved are 600 and 250 m s^{-1} . Compared with the previous results it appears that zinc sulphide is more erosion resistant than the selenide. The amount of cracking is less and the second impact site does not show significantly more damage than the first. The fracture labelled B is the same in each photograph.

Figure 31 illustrates the much more severe damage which results at an impact velocity of 900 m s^{-1} on zinc selenide. At this velocity there is subsurface damage in the central region and "cone" and radial cracks have formed.

During the course of the work three amber coloured samples were supplied by Dr. W.F. Adler (Effects Technology Inc., Santa Barbara, California). The dimensions of the specimens were $25 \times 25 \times 18 \text{ mm}$. The impact surface was polished and no scratches were visible with the naked eye. No information was available on composition, deposition temperature, grain size and orientation of the columnar grains relative to the impact surface, but these will no doubt be described when Dr. Adler reports. A series of single and multiple impacts were made and these are described below.

Single Impact

Two examples of the damage produced at 300 m s^{-1} impact velocity are shown in Figure 32. The damage consists of a ring of small cracks around the central zone. The density of cracks decrease with radial distance but their length and depth increases.

A remarkable feature is the growth of the cracks associated with the polishing scratches (see Figure 32b, where it is particularly pronounced). These develop following interaction with the Rayleigh wave travelling along the surface. These cracks, or series of cracks, usually follow the line of the scratch and propagate into the material at an angle of $\sim 45^\circ$ with the surface. This contrasts with the small cracks in the inner ring which are more nearly normal to the surface. Further examples, of the effect of polishing damage appear in later figures. No material removal occurred at the intersections of the cracks and the surface at this velocity suggesting that the step height across the crack is very small.

Impact sites for impact velocities of 400 m s^{-1} are shown in Figures 33 a and b. The number and depth of the cracks has increased. For impact

velocities of 500 (Figures 34 a and b) and 600 m s^{-1} , (Figure 35) the density of small cracks in the inner damage ring increases even more. The nature of the damage has not changed over the velocity region studied, though clearly the effect of polishing damage is more pronounced.

Double Impact

The growth of the damage in an impact site caused by an adjacent second liquid jet impact was studied for an impact velocity of 500 m s^{-1} . Again two examples are illustrated. Figures 36a and 37a show the single impact at 500 m s^{-1} . The damage after the second impact is shown in Figures 36b and 37b. The growth of the cracks of the first damage ring is relatively small. Several new cracks are formed which are orientated at $\sim 90^\circ$ with the old cracks which shows that the Rayleigh wave only expands flaws which are about normal with the propagation direction.

Figure 38a,b,c show the sequence for triple impact with the impact centres at the corners of an equilateral triangle. The numbers give the order of firing. Detailed examination shows that some extension of earlier cracks occurs and that after multiple impact cracks of several millimetres length can be found (made up of several short cracks joining together). In each case new cracks form and these individual circumferential cracks are not noticeably longer than for the first impact.

"Talysurf" profilometer measurements could have given information about plastic deformation in the central zone. Etching would have revealed the nature of the fracture. Cross-sectioning would have given useful information concerning depth and orientation of the cracks. However, these particular specimens had to be returned to Dr. W.F. Adler for these types of study.

4. CONCLUSIONS

The jet method allows a rapid assessment of the rain erosion behaviour of a specimen. The research discussed here was concerned with improving jets from 0.4 and 0.8mm orifice chambers. These jets are particularly

useful since they can simulate, with reasonable accuracy, drop impact in the size range 2 to 4mm for a wide range of velocities (Figure 3). The photographic records (Figures 8 and 9) show that the jets have smooth, slightly curved, front surfaces. This coupled with the fact that the "water hammer" pressures are controlled by the initial stage of impact and not by the much lower (incompressible flow) pressures from the tail of the jet, allows the jets to simulate drop impact.

The hydraulic strength test has proved to be an extremely useful technique for quantifying damage introduced into materials by impact. It provides an inexpensive and rapid method for ranking materials for their rain erosion resistance (Field et al, 1977, 1979).

The damage marks produced by jets on zinc sulphide and zinc selenide show close similarities with those produced by spherical drops (Hackworth et al, 1977, Hackworth 1979).

The specimens provided by Dr. Adler appeared superficially good, but there were enough defects left after grinding and polishing to dominate the damage. Surface preparation and possibly the application of suitable protective layers would appear to be worthy of further study.

FIGURE CAPTIONS

1. Schematic diagram of jet method.
2. Nozzle for jet production. This nozzle is basically very simple and different diameter jets can be obtained by varying the orifice diameter d. In some situations it is best to have the water interface at the E position (orifice empty) in others at the F (full) position (Field et al. 1974, 1979). For optimum jets of small diameter new nozzles have been designed (see text).
3. Equivalent drop size as a function of impact velocity for jets from the nozzle illustrated in figure 3 for three nozzle diameters. Intermediate values can be found by interpolation.
4. Original nozzle designs from the work of Brunton (1959). The 60° nozzle (4c) was the one adopted for our earlier experiments (figure 2).
5. New nozzle designs tested in the present work. Orifice diameters of 0.4 and 0.8 mm were tested. Figure 5b is the "curved" chamber.
6. Nomenclature for damage site dimensions (in text).
7. Damage dimensions (see fig. 6 for nomenclature) for (a) the "old" 0.8 mm nozzle (fig. 2) and (b) the new curved nozzle at a stand-off distance of 10 mm. The new design shows much less scatter.
8. A single shot high-speed photograph of a high velocity jet produced from a 0.8 mm nozzle. The central core of liquid is coherent. The umbrella shape is due to a cloud of droplets; these droplets do not contribute to the damage.
9. Imacon sequences taken with a framing interval of 1 μ s for (a) 1.6 mm (b) 0.8 mm and (c) 0.4 mm nozzles. The grids are to aid the velocity measurement. Note the jets have smooth, slightly curved, fronts. This is basically why they simulate liquid drop impact so well.
10. Jet velocity versus stand-off distance for 0.4 mm 45° nozzle (fig. 5a) at different firing pressures. Plateau regions reached for stand-off

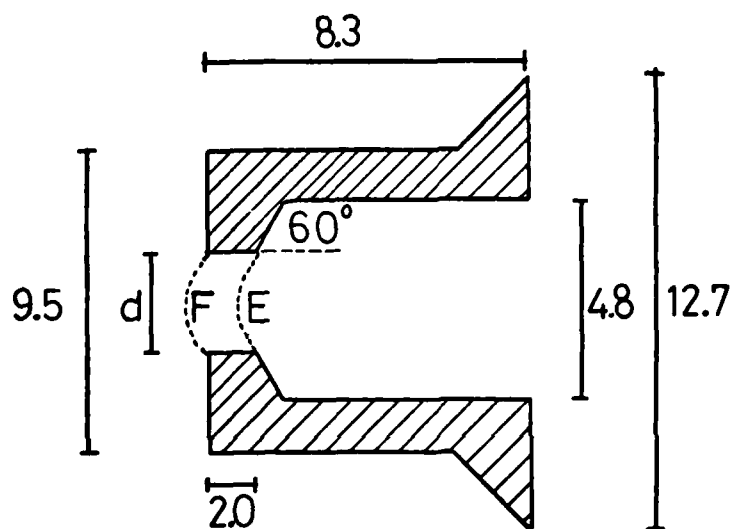
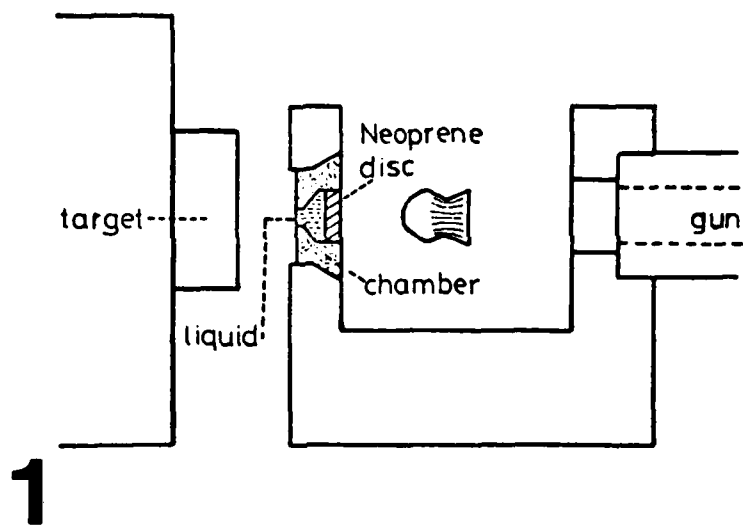
distances of about 10 mm.

11. As for fig. 19, but for 0.8 mm curved nozzle (fig. 5b).
12. As for fig. 11, but for 1.6 mm 60° nozzle (fig. 2).
13. Velocity versus firing pressure for 0.4 mm 45° nozzle (fig. 5a).
It is compared with earlier data (Rickerby 1976) for 60° nozzle (fig. 2)
14. Data for 0.8 mm curved nozzle (fig. 5b) compared with earlier data for 60° nozzle (fig. 2).
15. Nozzle with hardened stainless steel momentum exchanger: this cylinder has a length of 4.0 mm.
16. Arrangement as in figure 15 but with extra block (12 x 12 x 21 mm).
17. Velocity versus firing pressure for 0.4 mm 45° nozzle (fig. 5a).
Curve 1 is without any form of momentum exchanger (as in fig. 13).
Curve 2 is with the arrangement of figure 15. Curves 3 and 4 as with the arrangement of figure 16 with aluminium and steel blocks respectively.
18. As for figure 17 but for 0.8 mm curved nozzle (fig. 5b).
19. Glass discs (25 mm radius) broken in the hydraulic tester. Failure initiated at points F, (a) at the support and (b) away from the support where the stress field is well defined.
20. Scale schematic diagram of the hydraulic strength test apparatus.
21. Radial distribution of (a) σ_r and (b) σ_θ for various values of r_1/r_2 each normalised to the central value when $r_1 = r_2$ (σ_0).
22. Comparison between theory and experiment for the strain distribution (divided by the pressure) across (a) 3 mm thick and (b) 6 mm thick discs.
○ - radial component, ● - circumferential component.
23. Fracture stress of hot-pressed silicon nitride as a function of impact velocity for impacts by 3 mm diameter water jets.
24. Schematic diagram showing the pit formed by plastic deformation and radial cracks produced by Vickers indentations.

25. Typical results of plotting $\frac{a^{3/2}}{x}$ versus L. The inverse of the slope gives $K_{IC} = 4.9 \text{ MNm}^{-3/2}$.
26. Fracture stress data of figure 5 replotted in terms of the equivalent flaw size, c.
27. Liquid jet impact of zinc selenide with a 600 m s^{-1} jet from a 0.4 mm nozzle. The equivalent drop size is 2.4 mm. (a) upper picture single impact (b) lower picture, a second impact to the right of that shown in (a). The feature labelled A is the same for both.
28. Enlarged view of the damage for impacts on zinc selenide (a), at left; 600 m s^{-1} . The feature labelled A is the same as in fig. 19. (b) 250 m s^{-2} .
29. Liquid jet impact on zinc sulphide. Identical experiments to those illustrated in fig. 19 so direct comparison is possible.
30. Liquid jet impact on zinc sulphide. Identical experiments to those illustrated in fig. 20. Feature labelled B is the same as in fig. 21.
31. Liquid jet impact at a velocity of 900 m s^{-1} on zinc selenide. No longer an undamaged central region. Cone and radial cracks have formed.
- 32a and b. Zinc sulphide, 300 m s^{-1} , equivalent drop size 2.3 mm. The effect of polishing damage is particularly noticeable in b.
- 33a and b. ZnS, 400 m s^{-1} , equivalent drop size 2.0 mm (a) shows an impact mark where surface preparation damage was small. (b) an area where surface preparation damage was great.
- 34a and b ZnS, 500 m s^{-1} , equivalent to drop size 2.0 mm.
35. ZnS, 600 m s^{-1} , equivalent drop size 2.3 mm. The density of cracks in the main ring is very intense.
36. ZnS, double impact at 500 m s^{-1}
37. ZnS, double impact at 500 m s^{-1}
38. ZnS, triple impact (1,2 and 3) at 500 m s^{-1} .

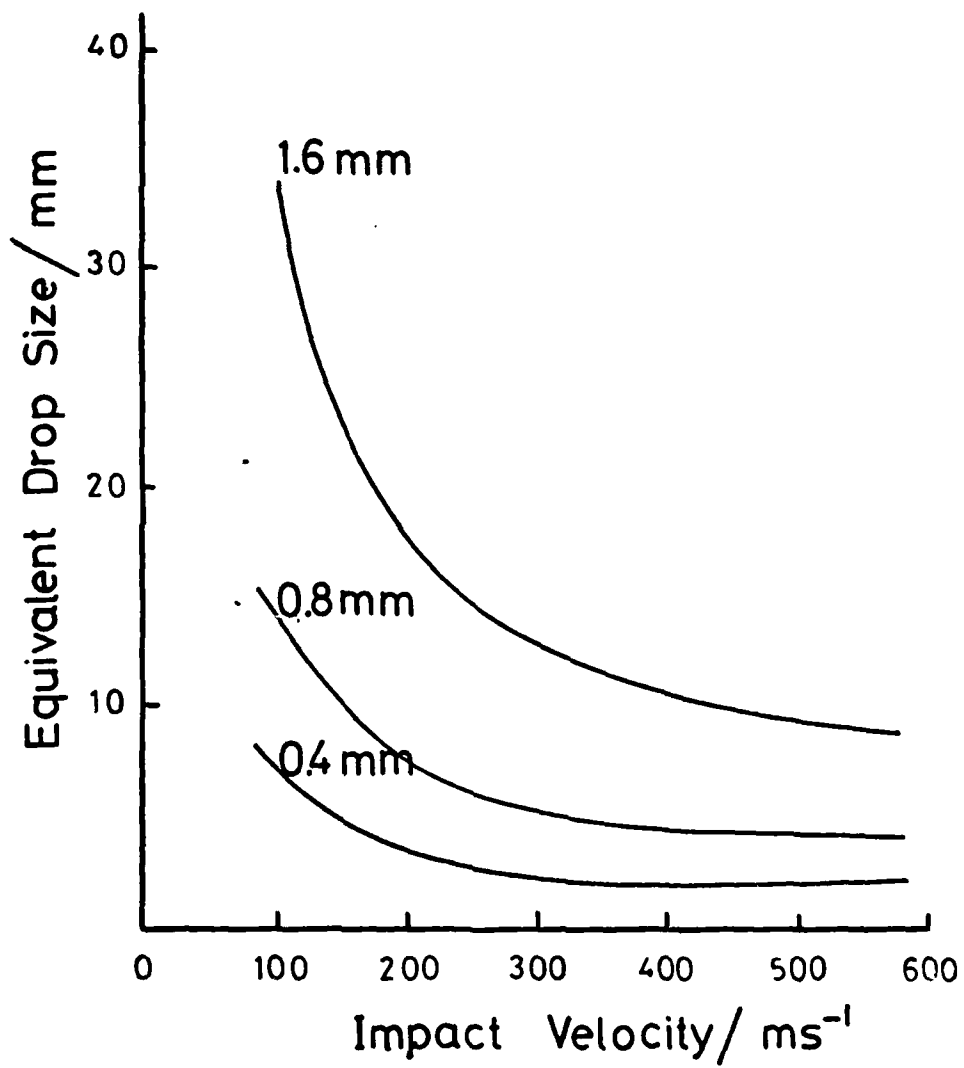
REFERENCES

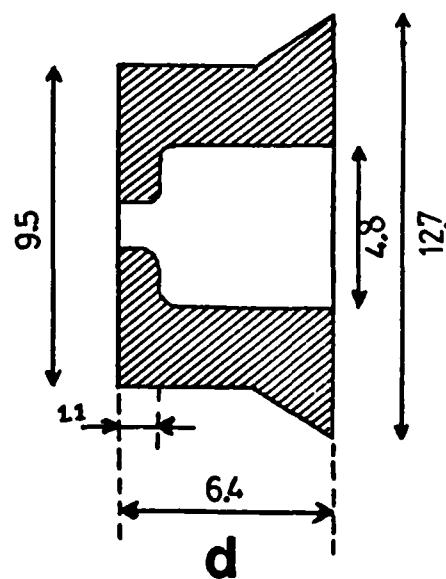
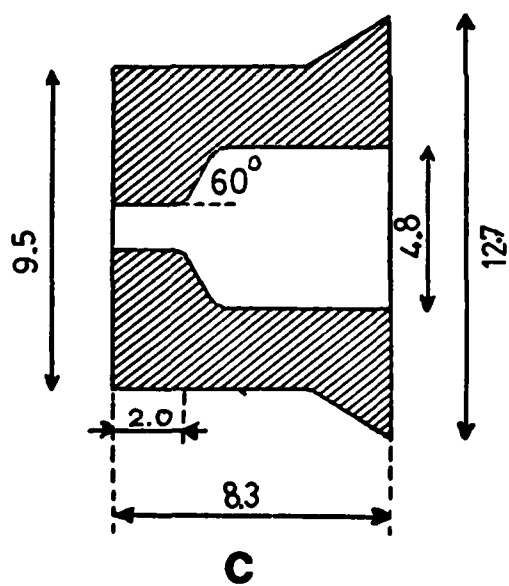
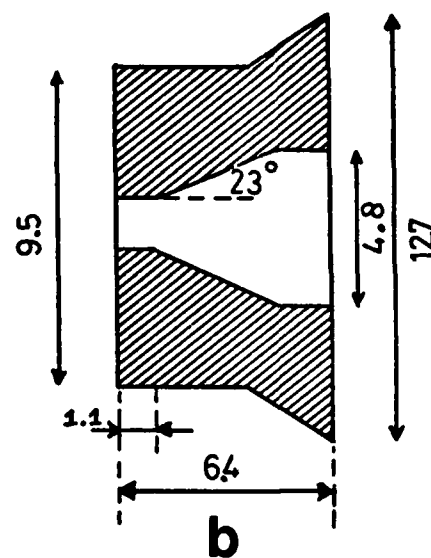
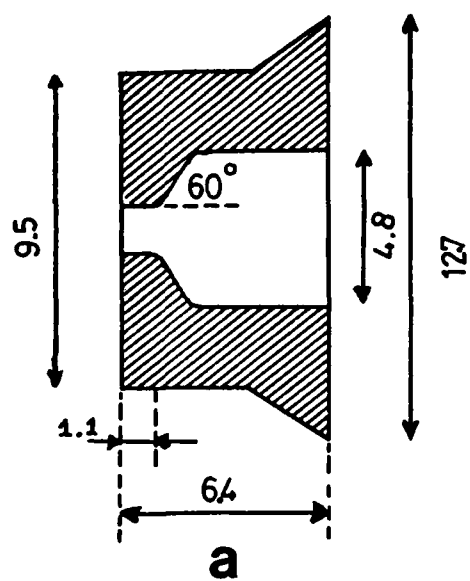
- Bowden, F.P. and Brunton, J.H., 1958, Nature 181, 873.
- Bowden, F.P. and Brunton, J.H., 1961, Proc. Roy. Soc., A263, 433
- Bowden, F.P. and Field, J.E., 1964, Proc. Roy. Soc., A282, 331.
- Brunton, J.H., 1959, Ph.D. Thesis, University of Cambridge.
- Camus, J.-J., 1971, Ph.D. Thesis, University of Cambridge
- Evans, A.G., 1978, Private Communication
- Field, J.E., 1962, Ph.D. Thesis, University of Cambridge
- Field, J.E., 1967, 2nd Int. Conf. on Rain Erosion and Allied Phenomenon, Meersburg, West Germany, p593.
- Field, J.E., Camus, J.-J., Gorham D.A. and Rickerby D.H., 1974, Proc. 4th Int. Conf. on Rain Erosion, Meersburg, p395.
- Field, J.E., Camus, J.-J., Gorham D.A. and Rickerby, D.G., 1976, DR MAT REPORT 203 VR 55079.
- Field, J.E., Gorham, D.A. and Rickerby, D.G., 1979(a), Proc. ASTM Erosion Conf. Vail Colorado, Oct., 1977, ASTM, STP 664, W.F. Adler, Ed., p.298.
- Field, J.E., Gorham D.G., Hagan, J.T., Matthewson, M.J., Swain, M.V. and van der Zwaag, 1979(b), Proc. 5th Int. Conf. Erosion by Liquid and Solid Impact (ELSI V), Cambridge, 1979.
- Field, J.E. and Lesser M.B., 1977, Proc. Roy. Soc., A357, 143.
- Gorham, D.A., 1974, Ph.D. Thesis, University of Cambridge.
- Gorham, D.A. and Rickerby, D.G., 1975, J. Phys. E : Sci. Instrum. 8, 794.
- Kinoshita, T., 1976, Proc. 3rd Int. Symp. on Jet Cutting Tech., Chicago, USA.
- Lawn, B.R. and Fuller, E.R., 1975, J. Mater. Sci., 10, 2016
- Leach, S.J. and Walker G.L., 1966, Phil. Trans., A260, 295.
- Mansfield, E.H., 1963, J. Roy. Aero. Soc., 67, 671.
- Matthewson, M.J., 1976, Ph.D. Thesis, University of Cambridge.
- Rickerby, D.G., 1976, Ph.D. Thesis, University of Cambridge.
- Timoshenko, S., 1940, "Theory of plates and shells", 1st edn., Chapt.2, p.55, McGraw Hill, New York.
- Woodward, A.C., 1974, Ph.D. Thesis, University of Cambridge.



dimensions in mm

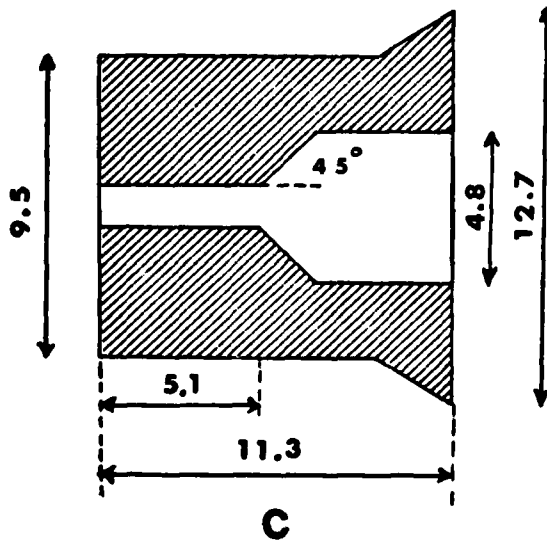
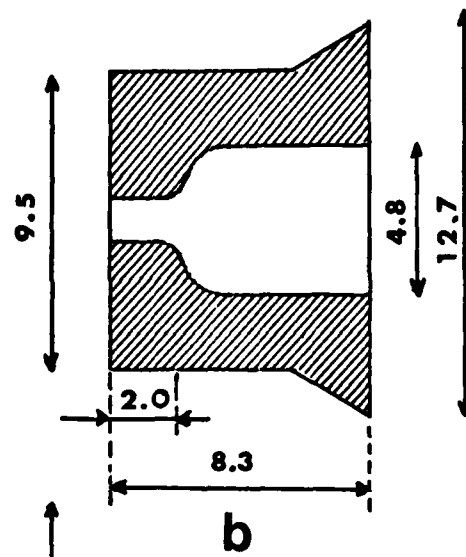
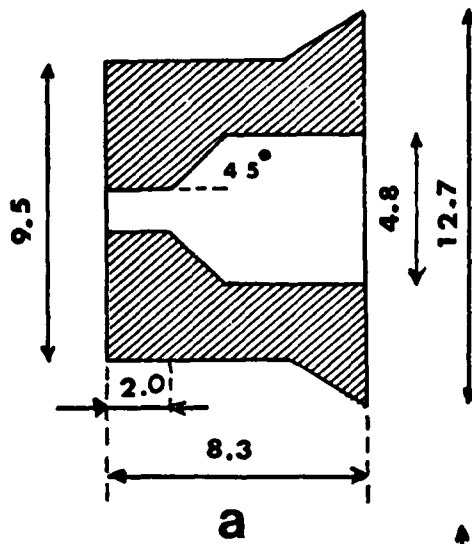
2

**3**



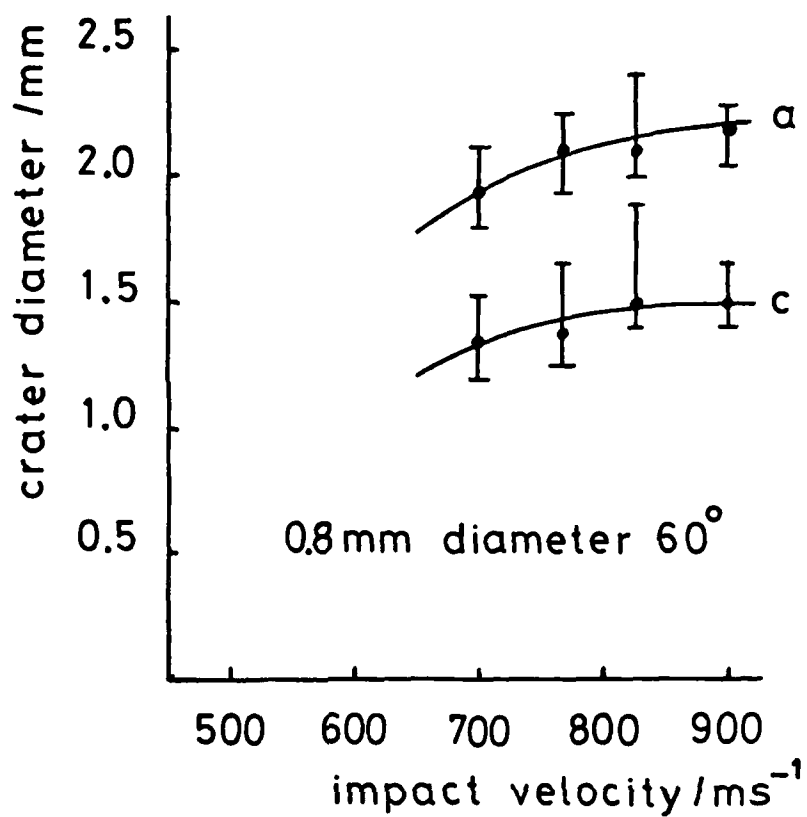
dimensions in mm

4

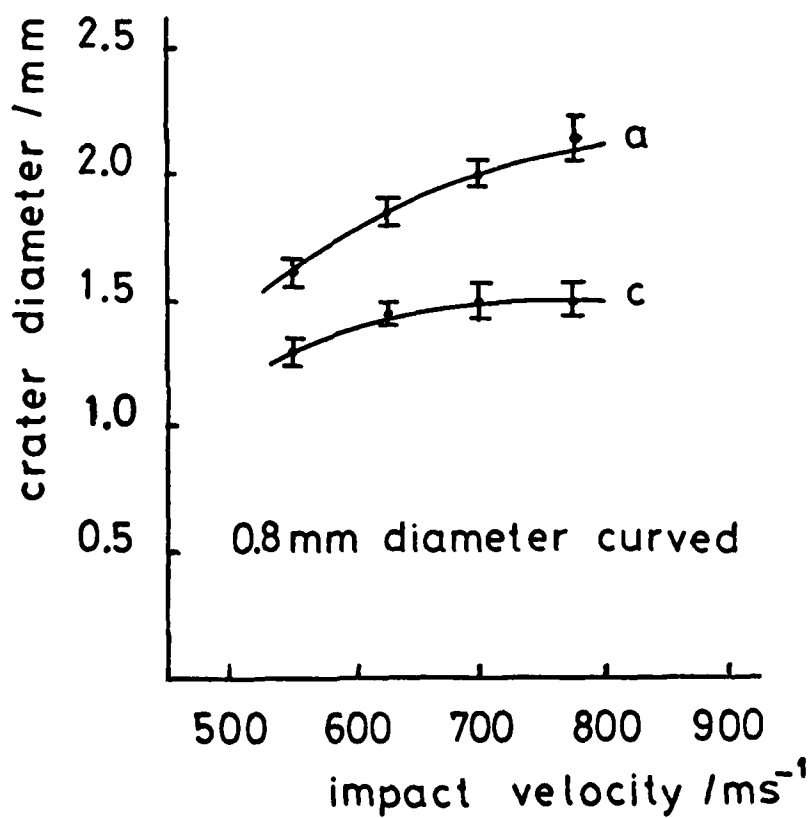


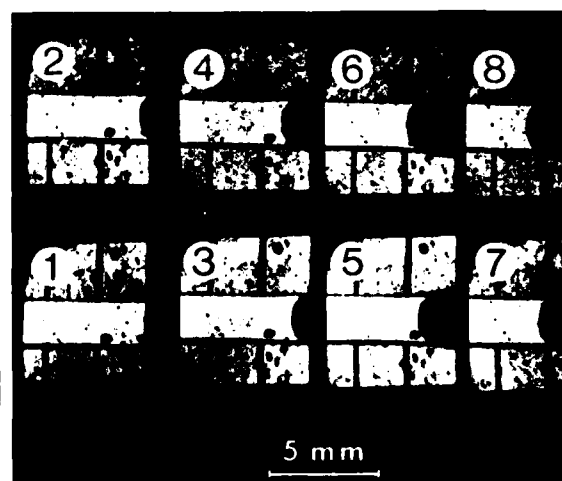
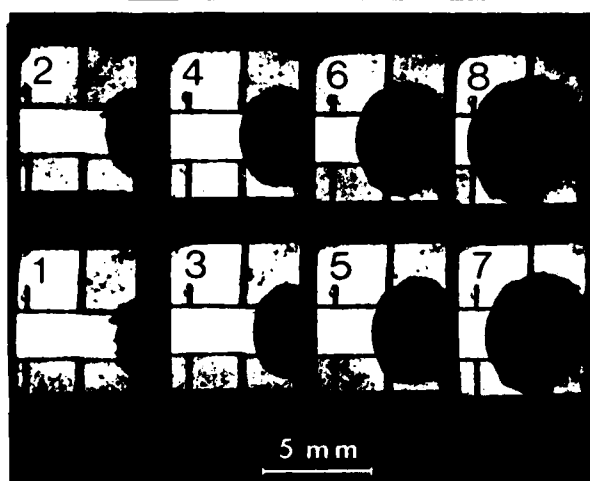
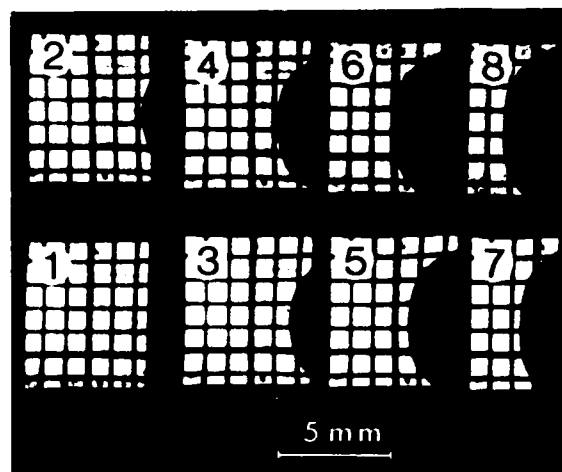
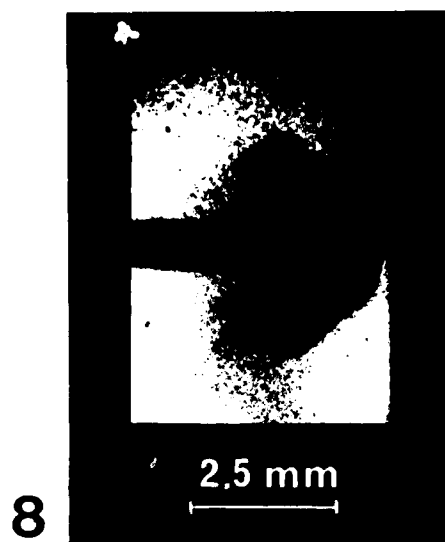
5

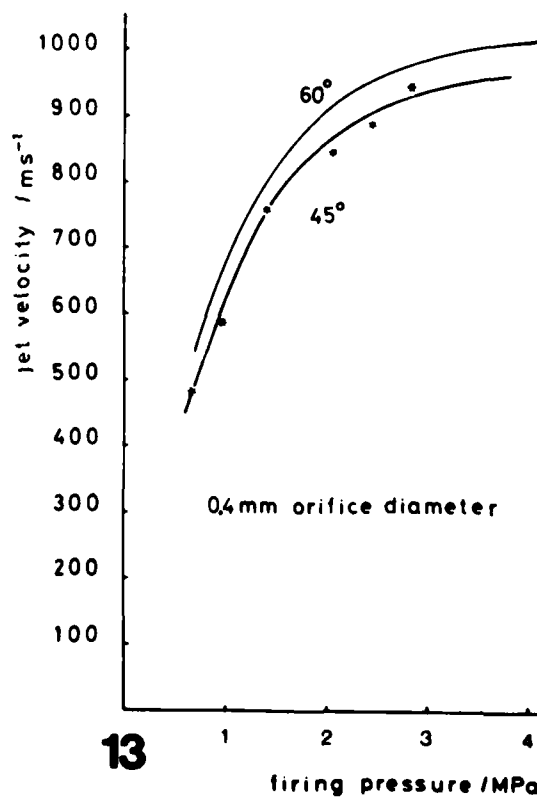
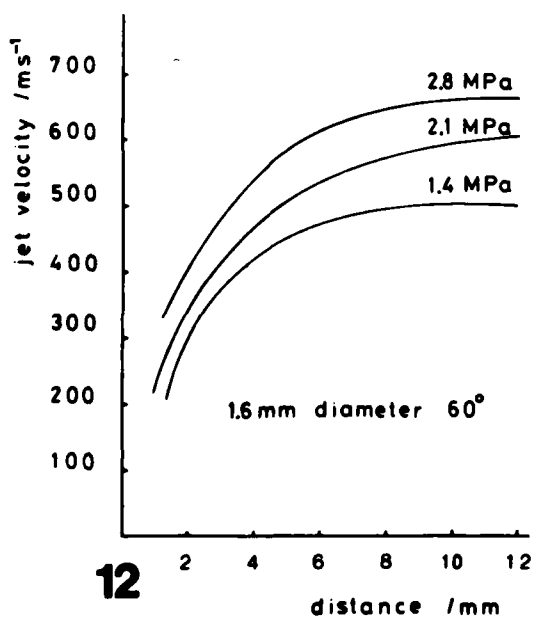
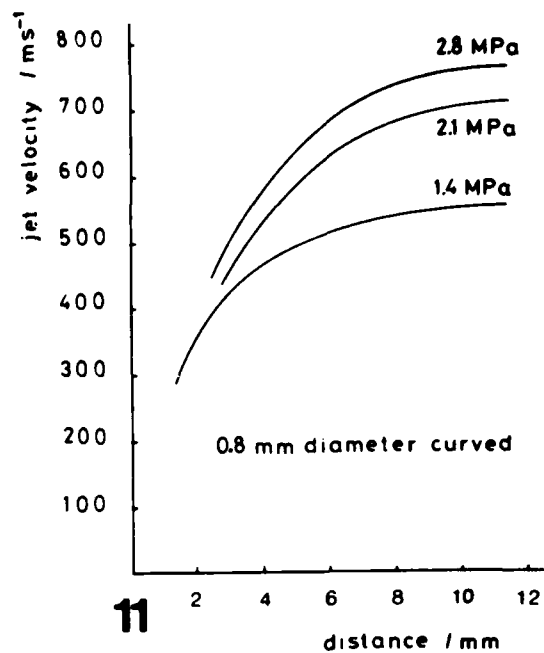
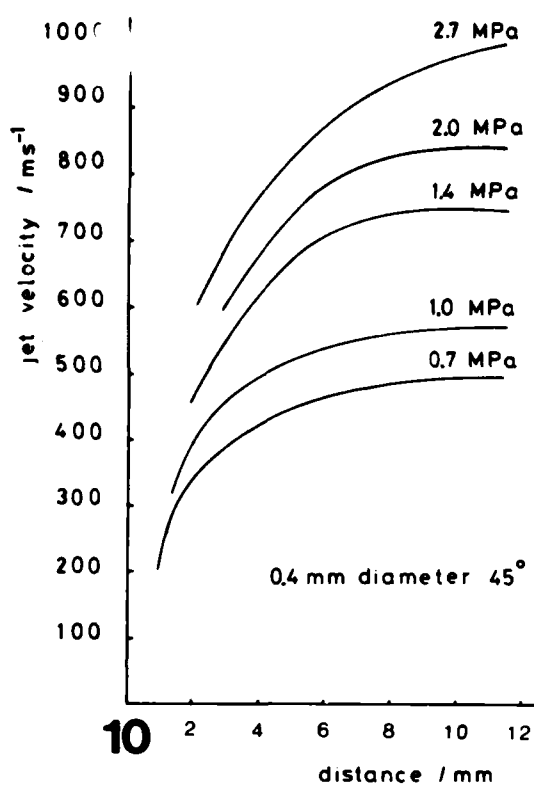
7a

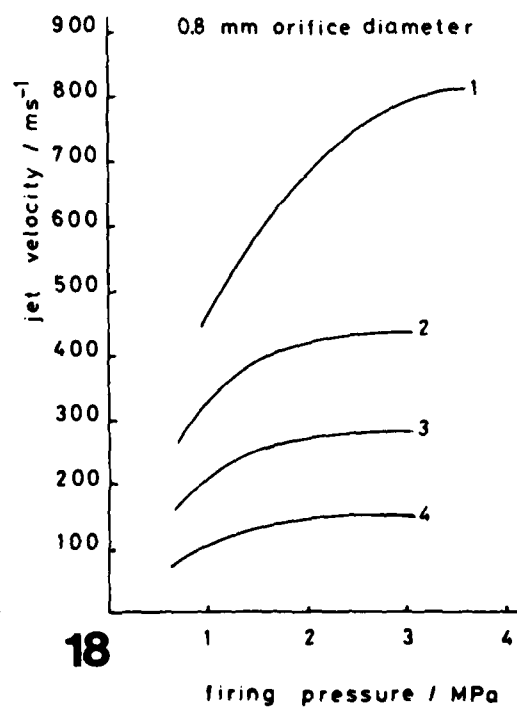
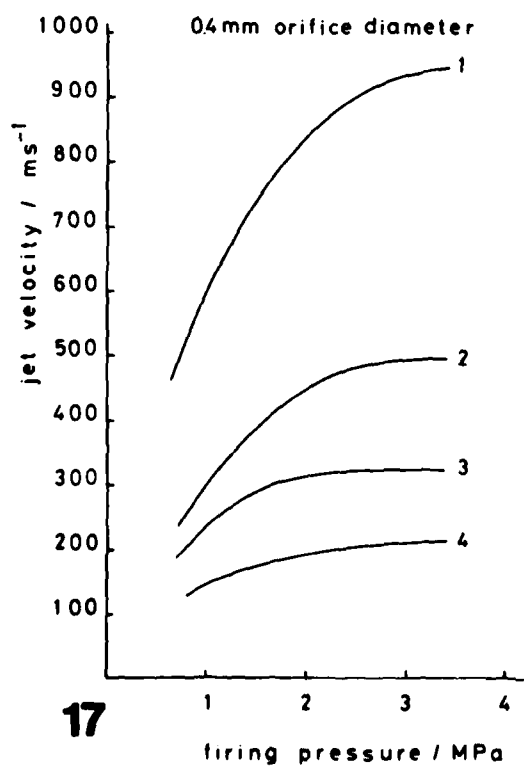
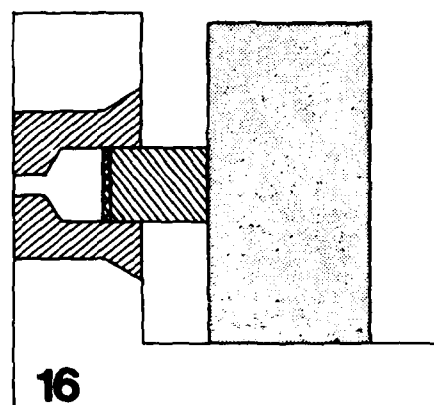
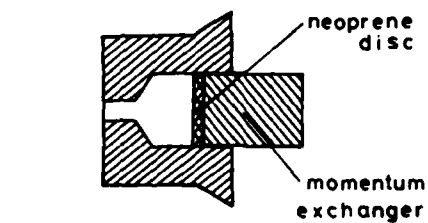
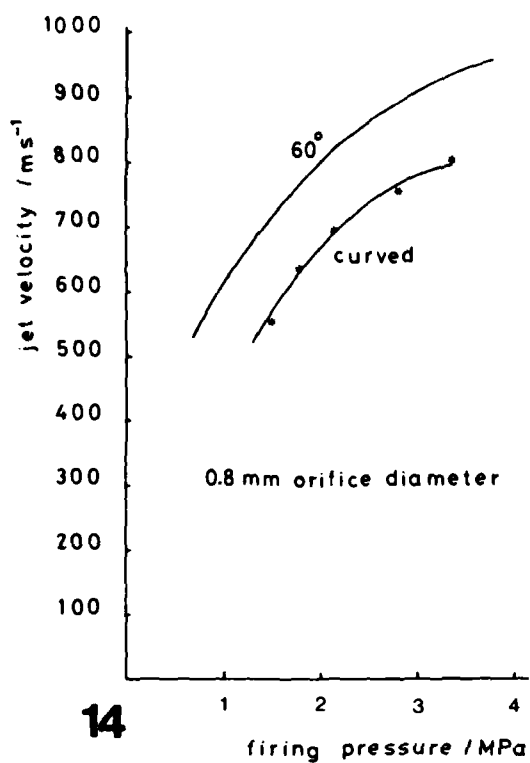


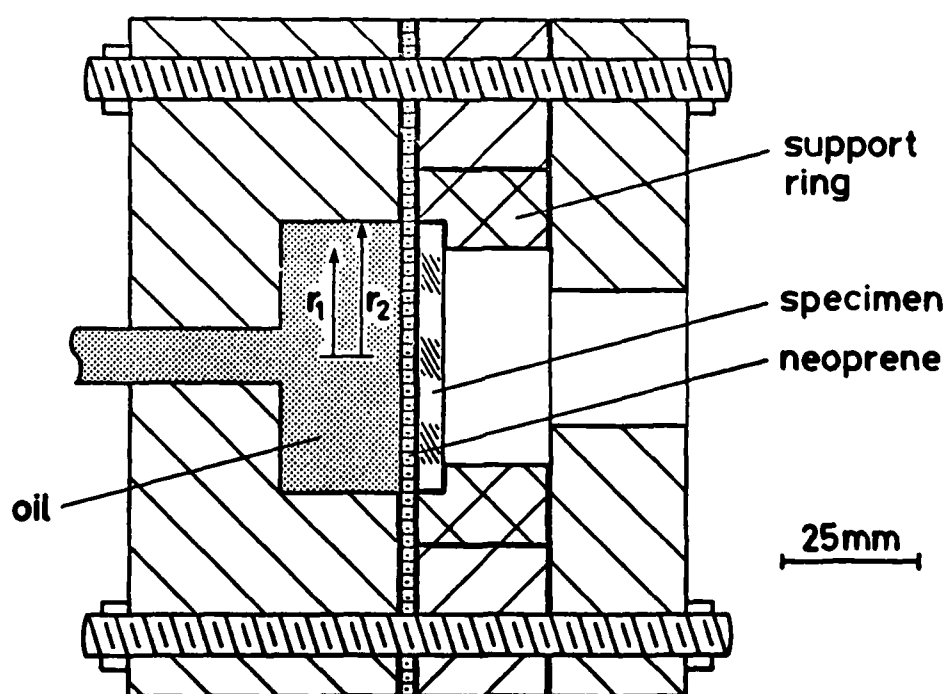
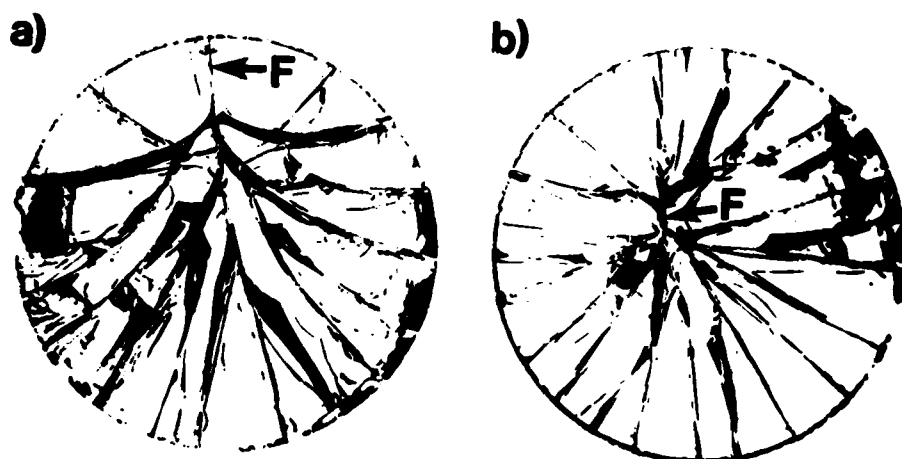
7b

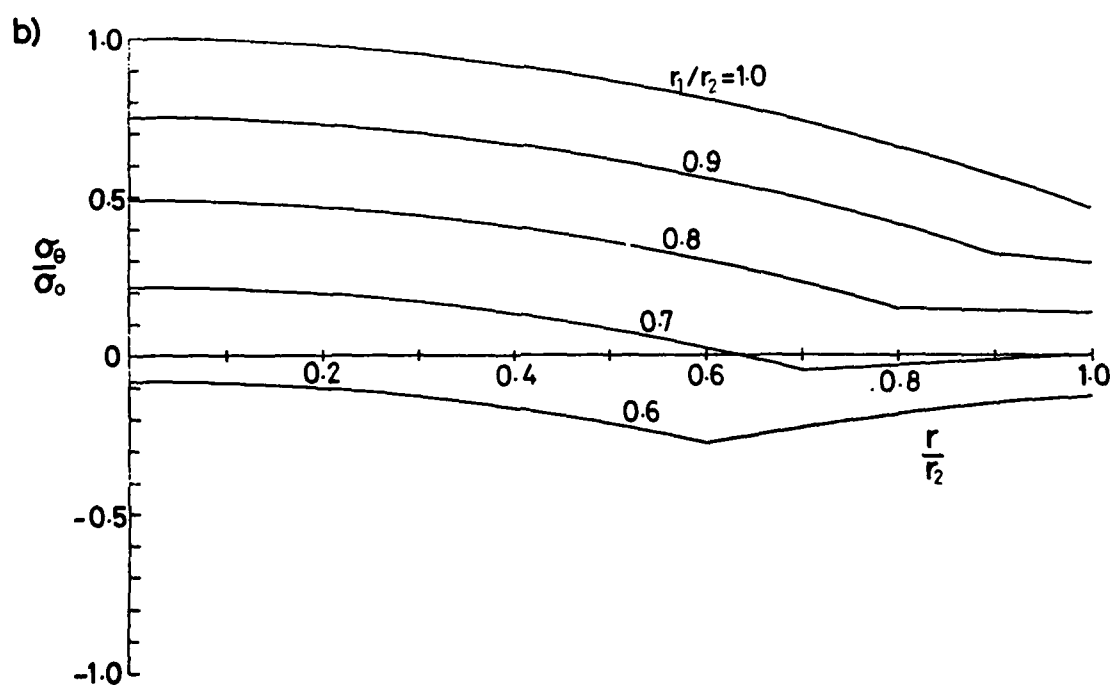
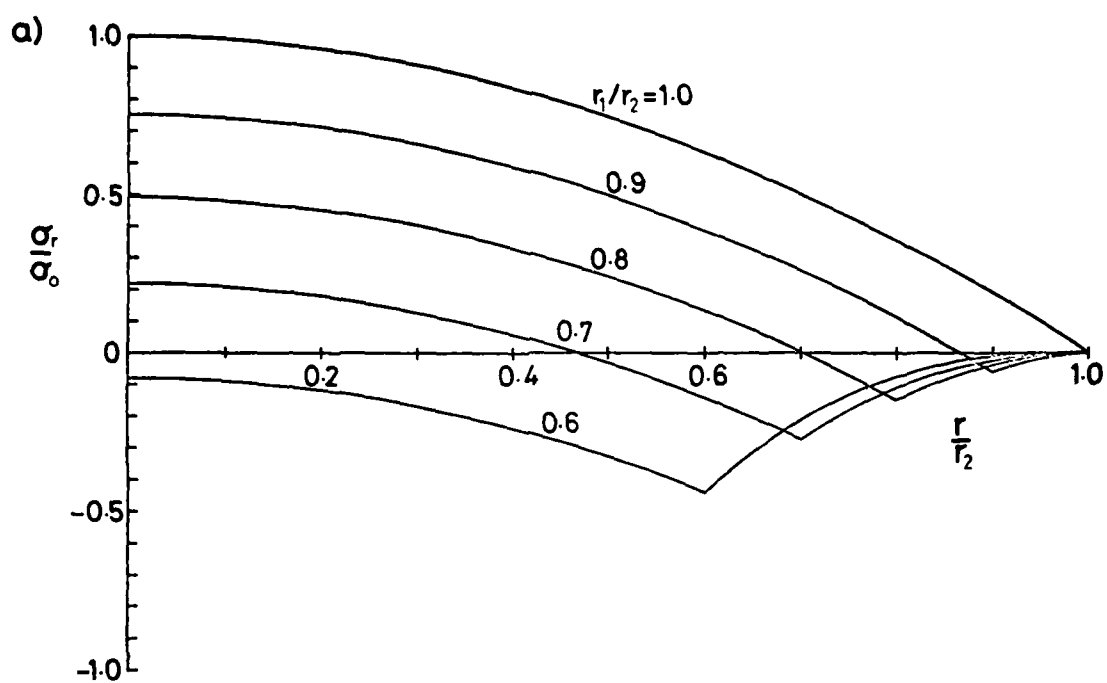


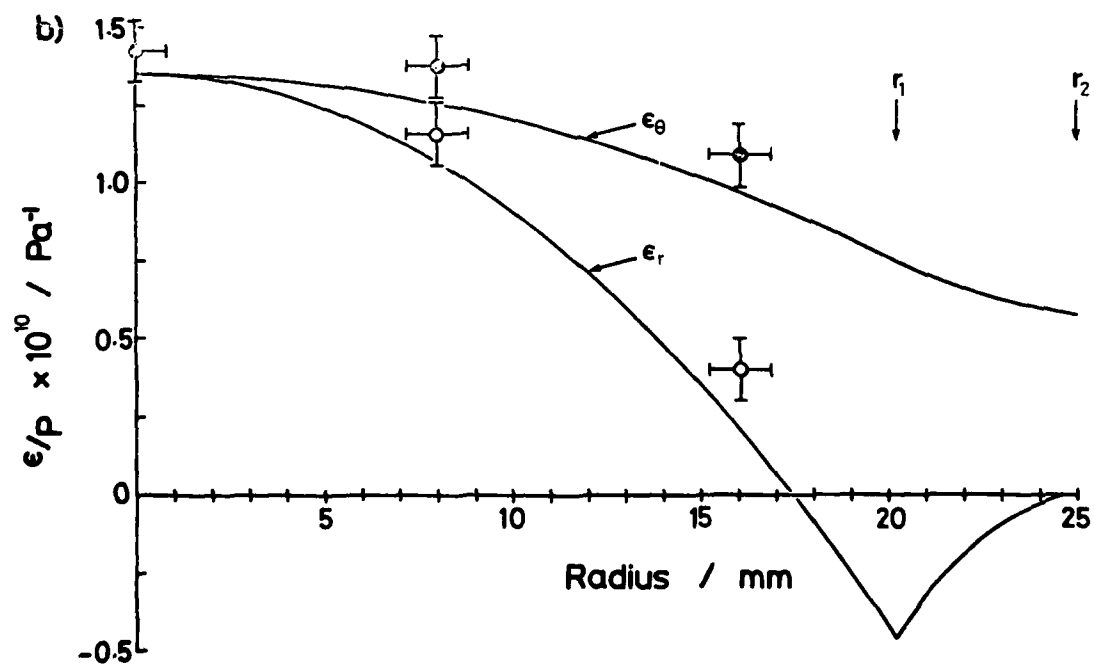
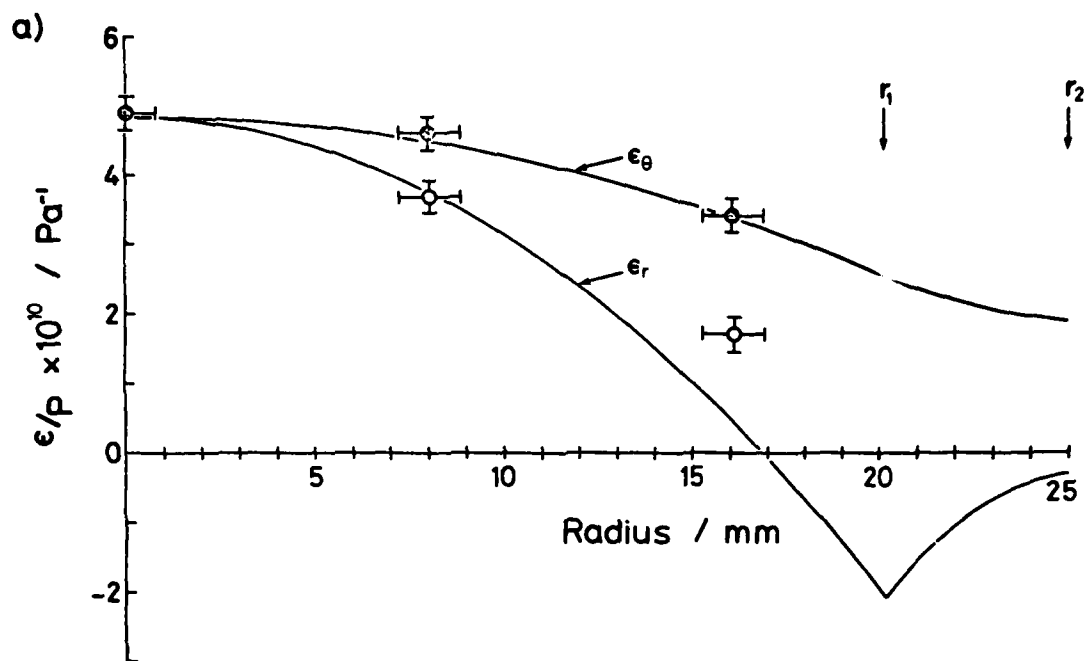


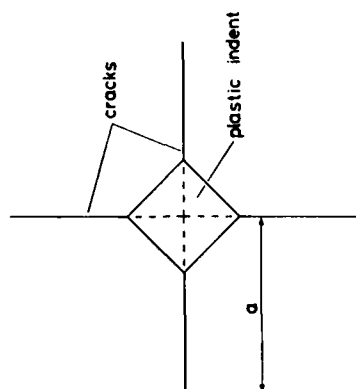




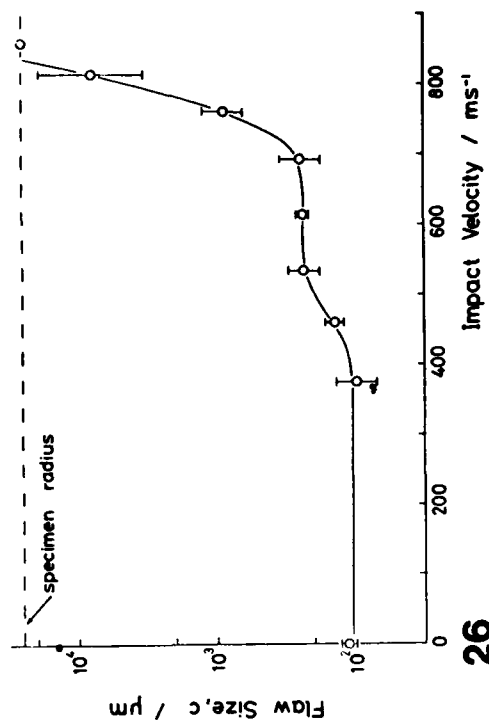




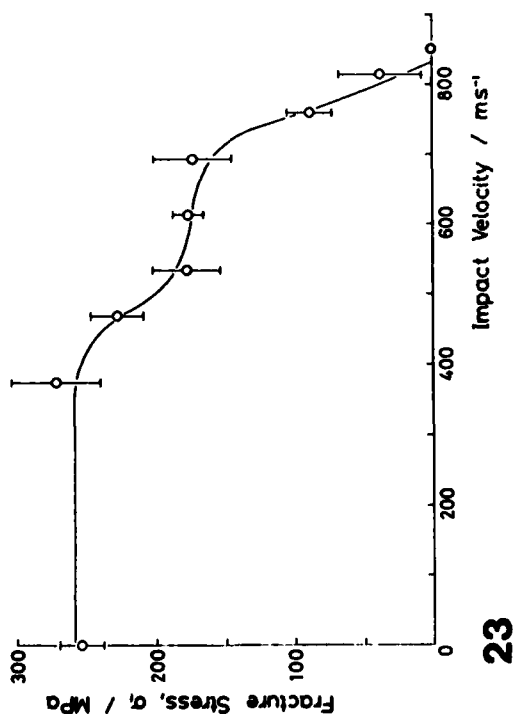




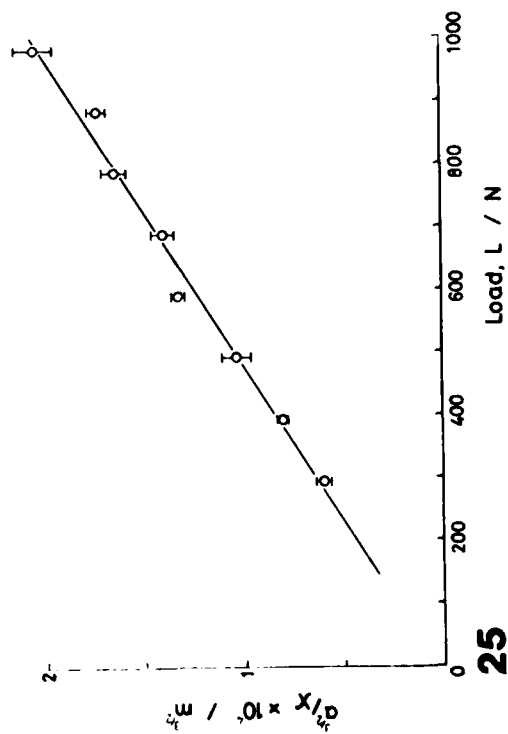
24



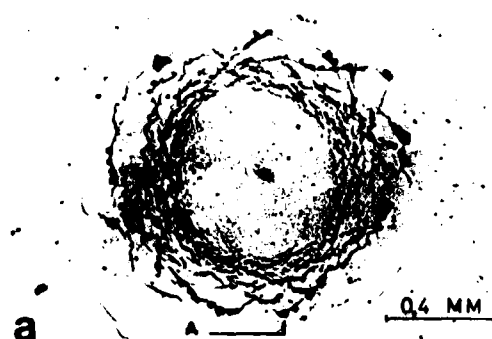
26



23



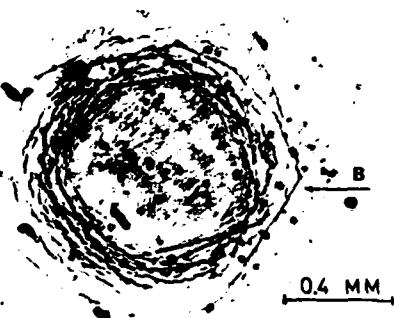
25



a



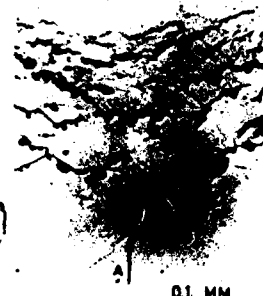
b
27



a



b
29



a
28

b

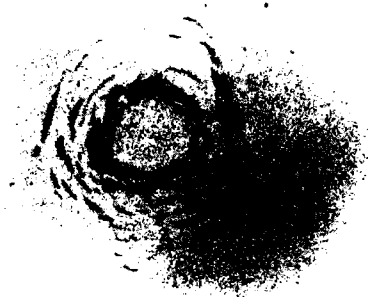


a
30

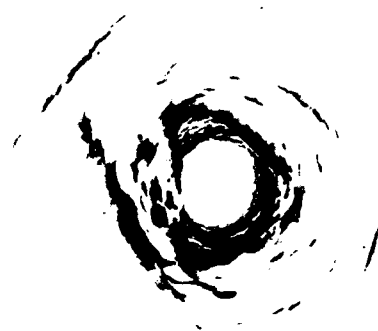


31

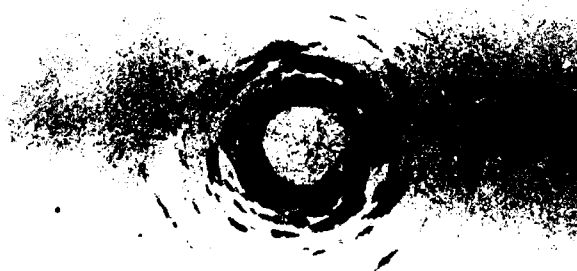
32a



b



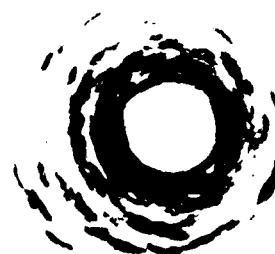
33a



b

1mm



**34a****b****35**

1 mm

A horizontal scale bar with vertical end caps, indicating a length of 1 mm.

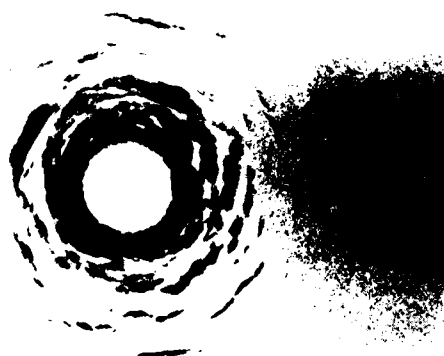
36a



b



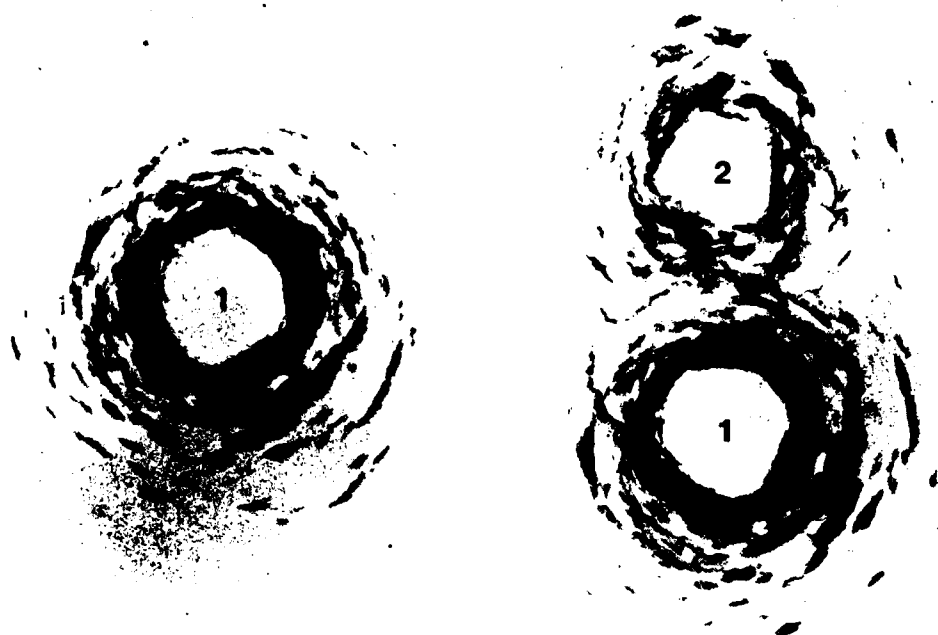
37a



b



1 mm



1 mm



38

— 8